CURRENT FLOW PATTERNS IN TWO-DIMENSIONAL ANISOTROPIC BISYNCYTIA WITH NORMAL AND EXTREME CONDUCTIVITIES

ROBERT PLONSEY AND ROGER C. BARR
Department of Biomedical Engineering, Duke University, Durham, North Carolina 27706

ABSTRACT Cardiac tissue has been shown to function as an electrical syncytium in both intracellular and extracellular (interstitial) domains. Available experimental evidence and qualitative intuition about the complex anatomical structure support the viewpoint that different (average) conductivities are characteristic of the direction along the fiber axis, as compared with the cross-fiber direction, in intracellular as well as extracellular space. This report analyzes two-dimensional anisotropic cardiac tissue and achieves integral equations for finding intracellular and extracellular potentials, longitudinal currents, and membrane currents directly from a given description of the transmembrane voltage. These mathematical results are used as a basis for a numerical model of realistic (though idealized) two-dimensional cardiac tissue. A computer simulation based on the numerical model was executed for conductivity patterns including nominally normal ventricular muscle conductivities and a pattern having the intra- or extracellular conductivity ratio along x, the reciprocal of that along y. The computed results are based on assuming a simple spatial distribution for V_m, usually a circular isochrone, to isolate the effects on currents and potentials of variations in conductivities without confounding propagation differences. The results are in contrast to the many reports that explicitly or implicitly assume isotropic conductivity or equal conductivity ratios along x and y. Specifically, with reciprocal conductivities, most current flows in large loops encompassing several millimeters, but only in the resting (polarized) region of the tissue; further, a given current flow path often includes four or more rather than two transmembrane excursions. The nominally normal results showed local currents predominantly with only two transmembrane passages; however, a substantial part of the current flow patterns in two-dimensional anisotropic bisyncytia may have qualitative as well as quantitative properties entirely different from those of one-dimensional strands.

INTRODUCTION

The object of this paper is to describe the current flow patterns that arise in uniform anisotropic two-dimensional syncytial tissue from an assumed action potential distribution (circular and elliptical isochrones). This study is motivated by an interest in the electrophysiological implications arising from the recently documented anisotropic and syncytial structure of cardiac tissue. The two-dimensional tissue behavior appears not to be a simple extension of one-dimensional cable theory except for (unlikely) special circumstances. This paper explores particularly the current flow patterns and their relationships that arise in two dimensions.

The experiments of Clerc (1) make clear that, with regard to cardiac muscle, all intracellular space behaves as if interconnected (syncytial), but with higher conductivity along the fiber axis than transverse to it. The interstitial space is also clearly interconnected; it too is anisotropic with higher conductivity along the fiber axis.

The structural contributions to the syncytial behavior are not completely understood, but appear to depend on the low-resistance gap junctions (mainly at the ends of interconnecting cells), the anastomosing cellular arrangement, as well as more isolated lateral junctions between cells. In addition to uncertainties in junctional structure there is also uncertainty in the quantitative electrophysiological properties of the junctions themselves (their conductance and capacitance).

The model that we consider is macroscopic; hence it avoids some of the uncertainties associated with the cellular details. For the model it is assumed that macroscopic conductivity parameters have been experimentally determined and are known. It is further assumed that the tissue can be characterized as two dimensional (either because the tissue is very thin or because excitation and structure have imposed uniformity along one coordinate axis). Because the viewpoint is global rather than cellular (discrete) it is convenient to consider both intracellular space and interstitial space to be continuous and described by the

Correspondence and reprint requests should be addressed to Dr. Robert Plonsey, Department of Biomedical Engineering, Duke University, Durham, NC 27706.

same coordinates (both spaces are necessarily congruent, or, as described by Schmitt (2), "interpenetrating domains"). The membrane separating the two regions must be similarly distributed throughout. Mathematically, this structure is characterized by the following equations, which are expressions of Ohm's law:

$$\bar{J}_i = -[g_{ix}\,\partial\Phi_i/\partial x\,\bar{a}_x + g_{iy}\,\partial\Phi_i/\partial y\,\bar{a}_y] \quad (1)$$

$$\bar{J}_o = -[g_{ox}\,\partial\Phi_o/\partial x\,\bar{a}_x + g_{oy}\,\partial\Phi_o/\partial y\,\bar{a}_y]. \quad (2)$$

In Eq. 1 the subscript i refers to the intracellular domain, with g_{ix} being the conductivity in the x direction and g_{iy} that in the y direction. Both conductivities have the dimensions of Siemans per millimeter (i.e., defined on the total space). Similar comments apply to Eq. 2 where the subscript o refers to the interstitial space. (In these equations Φ is the scalar electrical potential and $\bar{a}$ the unit vector.) Both spaces are coupled through transmembrane current where outflow from one region must equal inflow to the other. Mathematically this is expressed by

$$-\nabla \cdot \bar{J}_i = \nabla \cdot \bar{J}_o = I_v \quad (3)$$

where I_v is the transmembrane current per unit volume (dimensionally rather strange at first sight, but appropriate to the distributed model that is postulated). This basic formulation of the problem has been presented and discussed by previous investigators of syncytial tissue including Miller and Geselowitz (3) (who called the medium "bisyncytial"), Tung (4) (using the adjective "bidomain"), Roberts and co-workers (5, 6), and others who have implied these ideas. The electrotonic response to a point source of current has also been studied in syncytia and also results in a bidomain point of view. For example, Peskoff (7) provides solutions for isotropic three-dimensional syncytia. Eisenberg et al. (8) do so for both isotropic and anisotropic syncytial media under conditions of a point source of current with sinusoidal or steady current.

It should be noted at the outset that we are assuming the macroscopic behavior of cardiac tissue to reflect actual behavior of real tissue. Because of the nonlinear properties of excitable membranes the influence of the discrete junctions on propagation could be such that specific account of their influence is necessary (9). In the present simulation the junctions enter only through a contribution to the average conductivity parameters.

Description of Simulation

We assume the existence of a circular isochrone on a two-dimensional anisotropic tissue that is characterized through average conductivity parameters defined in a bidomain system. The goal of the simulation is a description of the patterns of current in the interstitial and intracellular domains as a function of anisotropy values. We shall see that, except when the anisotropy ratios are equal (i.e., $g_{ix}/g_{iy} = g_{ox}/g_{oy}$), the directions of current in the intracellular and interstitial space are not equal and opposite, so that rather complex nonintuitive patterns result. (Barr and Jakobbson (10), in fact, make the assumption that $\bar{J}_i = -\bar{J}_o$ without recognizing that the assumption is valid only under very special circumstances.)

The sections that follow examine the intracellular, transmembrane, and interstitial current densities from a given, instantaneous transmembrane action potential distribution $V_m(x, y)$. The action potential distribution is chosen to be that associated with a circular isochrone.

In real tissue, it is of course well known that current flow in the active region depends on nonlinear membrane properties controlling the relationship of current and voltage. The voltages and currents in the active region then cause currents and voltages elsewhere, and propagation may ensue. In this report, the intracellular, transmembrane, and interstitial current densities as they relate to tissue conductivities are the primary focus of interest.

To isolate the effects of changes in tissue conductivities, the procedure we used was to choose the values of $V_m(x, y)$ to be those values associated with an idealized action potential shape centered on a circular isochrone. (We are tacitly assuming that no physical laws are violated when $V_m(x, y)$ is chosen arbitrarily, a question that merits further study.) Choosing $V_m(x, y)$ had the effect of specifying the resulting effect of active membrane properties and therefore made it unnecessary, for this idealized case, to compute V_m. Furthermore, since the choice of the circular isochrone shape and $V_m(x, y)$ was the same along any radius of the circle, the resulting current flow patterns were also the same along any radius of the circle for isotropic conductivities. The currents varied along different radii for other conductivities directly as a reflection of the assumed conductivity properties (only), since V_m remained the same. Thereby the effects of changes in conductivities in this analysis were isolated from the concomitant effects of changes in V_m with propagation that would occur in real tissue. We viewed the isolation of the effects of the conductivities as desirable within the framework of this analysis since it allowed the effects of changes in conductivities to be seen separately.

It was not necessary for us to assume that a circular shape, if it existed in real tissue, would be preserved. In fact, Muler and Markin (11) and Plonsey and Rudy (12) show that the asymptotic shape of the isochrone ellicited from central stimulation depends on the conductivities. Those results indicate that such an isochrone will be circular only if the medium is isotropic. That is, although we use a circular isochrone as a means to compare current flow values and patterns for different sets of conductivities, such circular isochrones would not be expected in real tissue with these conductivities (except for isotropic conductivities). The question immediately arises, What isochrone shapes might be expected? While we have not attempted to answer this question within this report, we believe the mathematical derivations presented here can

provide a quantitative basis for forming an answer, and the numerical results presented here give a specific description of the ways in which the current flow patterns vary. Both the mathematical and numerical results show that it cannot be expected, in general, that the longitudinal intracellular and interstitial current magnitudes will be equal in magnitude and opposite in direction, as has been explicitly or implicitly assumed previously.

One consequence of the inequality of longitudinal intracellular and interstitial current magnitudes is the existence of component currents that follow complex pathways (i.e., to take advantage of the high conductivity directions). Furthermore, expressions for transmembrane current, which for a one-dimensional cable depend on the second spatial derivative of transmembrane potential at the same site, now require integration (with an appropriate weighting function) of second derivatives in x and y over the entire active tissue. We will examine the factors that influence the shape and strength of the weighting function and the conditions under which it degenerates into an impulse function (leading, thereby, to a generalization of one-dimensional cable theory).

Following derivation of equations, a numerical simulation will be described that shows examples of currents for cardiac tissue with different conductivity properties, including both isotropic and anisotropic conductivities.

MATHEMATICAL BASIS

Intracellular Potential, Φ_i

Eq. 3 contains an expression for the outflow of current (transmembrane current) per unit volume of intracellular (interstitial) space. Substituting Eqs. 1 and 2 into Eq. 3 gives explicit expressions for I_v, namely

$$I_v = g_{ix}\,\partial^2\Phi_i/\partial x^2 + g_{iy}\,\partial^2\Phi_i/\partial y^2 \tag{4}$$

$$I_v = -(g_{ox}\,\partial^2\Phi_o/\partial x^2 + g_{oy}\,\partial^2\Phi_o/\partial y^2). \tag{5}$$

Recognizing that the transmembrane potential, V_m, is defined as

$$V_m = \Phi_i - \Phi_o \tag{6}$$

permits one to replace Φ_o in Eq. 5 by $(\Phi_i - V_m)$. Then, equating Eq. 4 with Eq. 5, transposing all terms involving Φ_i to the left-hand side results in

$$(g_{ix} + g_{ox})\,\partial^2\Phi_i/\partial x^2 + (g_{iy} + g_{oy})\,\partial^2\Phi_i/\partial y^2 = g_{ox}\partial^2V_m/\partial x^2 + g_{oy}\,\partial^2V_m/\partial y^2. \tag{7}$$

Eq. 7 is a partial differential equation in Φ_i, where V_m (the postulated spatial action potential) plays the role of a source term.

We can solve Eq. 7 if it is first transformed to Poisson's equation. This is accomplished using the following substitutions

$$X = x/(g_{ix} + g_{ox})^{1/2}, \qquad Y = y/(g_{iy} + g_{oy})^{1/2} \tag{8}$$

which converts Eq. 7 into

$$\partial^2\Phi_i/\partial X^2 + \partial^2\Phi_i/\partial Y^2 = -\left[\frac{g_{ox}}{g_{ix} + g_{ox}}\,\partial^2V_m/\partial X^2 + \frac{g_{oy}}{g_{iy} + g_{oy}}\,\partial^2V_m/\partial Y^2\right]. \tag{9}$$

The integrated formal solution of Poisson's Eq. 13 for Eq. 9 is

$$\Phi_i(X, Y) = \frac{1}{4\pi}\int\left[\frac{g_{ox}}{g_{ix} + g_{ox}}\,\partial^2V_m/\partial X'^2 + \frac{g_{oy}}{g_{iy} + g_{oy}}\,\partial^2V_m/\partial Y'^2\right] + \{\log[(X - X')^2 + (Y - Y')^2]\}\,dX'dY' \tag{10}$$

where the integration variables are primed, and the unprimed variables denote the point at which Φ_i is evaluated (i.e., the field point). Eq. 8 can be substituted into Eq. 10 to recover the original variables

$$\Phi_i(x, y) = \frac{1}{4\pi}\int[g_{ox}\partial^2V_m/\partial x'^2 + g_{oy}\partial^2V_m/\partial y'^2] \log\left[\frac{(x - x')^2}{g_{ix} + g_{ox}} + \frac{(y - y)'^2}{g_{iy} + g_{oy}}\right]\frac{dx'dy'}{(g_{ox} + g_{ix})^{1/2}(g_{oy} + g_{iy})^{1/2}}. \tag{11}$$

Transmembrane Current Density, I_v

An expression for the transmembrane current can be obtained by substituting Eq. 11 into Eq. 4. The result is

$$I_v = \frac{1}{4\pi G}\int[g_{ox}\partial^2V_m/\partial x'^2 + g_{oy}\partial^2V_m/\partial y'^2] \cdot\left[D_t^2\left\{\log\left[\frac{(x - x')^2}{G_x} + \frac{(y - y')^2}{G_y}\right]\right\}dx'dy'\right] \tag{12}$$

where

$$D_t^2 \equiv g_{ix}\partial^2/\partial x^2 + g_{iy}\partial^2/\partial y^2 \tag{13}$$

$$G_x = g_{ix} + g_{ox} \tag{14}$$

$$G_y = g_{iy} + g_{oy} \tag{15}$$

$$G = (G_xG_y)^{1/2}. \tag{16}$$

Carrying out the differential operations results in

$$I_v = \frac{(\lambda_x - \lambda_y)}{2\pi G(1 + \lambda_x)(1 + \lambda_y)}\int[g_{ox}\partial^2V_m/\partial x'^2 + g_{oy}\partial^2V_m/\partial y'^2] \left\{\frac{\dfrac{(x - x')^2}{G_x} - \dfrac{(y - y')^2}{G_y}}{\left[\dfrac{(x - x')^2}{G_x} + \dfrac{(y - y')^2}{G_y}\right]^2}\right\}dx'dy' \tag{17}$$

where

$$\lambda_x = g_{ox}/g_{ix} \qquad \lambda_y = g_{oy}/g_{iy}. \tag{18}$$

Note that Eq. 17 implies behavior that differs from a simple extrapolation of one-dimensional cable theory. That is, except for the special cases to be described presently, Eq. 17 shows that contributions to the transmembrane current at some point (x, y) depend on the second derivative behavior of V_m (viewed as a "source") everywhere in the active region, not simply at the same point. In simulations to be presented we will observe that anisotropy can cause substantial (additional) circulating currents whose coupling is reflected by the Eq. 17.

Evaluation of I_v for Equal Anisotropy Ratios

When the anisotropy rates are equal $(g_{ox}/g_{oy} = g_{ix}/g_{iy})$ then $\lambda_x = \lambda_y = \lambda$ (an isotropic medium is a special case where $\lambda_x = \lambda_y = \lambda = 1$). In this case the integral in Eq. 17 equals zero except possibly in the region $x = x'$, $y =$

y' where the weighting function in the braces is singular. The contribution from an ϵ neighborhood of (x, y) can be most easily explored starting with Eq. 12. If in addition the transformation

$$X = x/(g_{ix})^{1/2} \qquad Y = y/(g_{iy})^{1/2} \tag{19}$$

is made then

$$I_v = \frac{(g_{ix}g_{iy})^{1/2}}{4\pi G} \int_\epsilon [g_{ox}\partial^2 V_m/\partial x'^2 + g_{oy}\partial^2 V_m/\partial y'^2] \cdot \nabla_t^2 \{\log [(X - X')^2 + (Y - Y')^2]\}\, dX'dY' \tag{20}$$

where $\nabla_t^2 \equiv \partial^2/\partial X'^2 + \partial^2/\partial Y'^2$, and the integral is over an ϵ region surrounding $X' = X$ and $Y' = Y$. The Laplacian of the quantity in the braces is known to be a delta function (the log function is a two-dimensional Green's function) whose integral is 4π (13). Consequently for equal anisotropy ratios,

$$I_v = \left(\frac{1}{1 + \lambda}\right)(g_{ox}\partial^2 V_m/\partial x^2 + g_{oy}\partial^2 V_m/\partial y^2). \tag{21}$$

So, for equal anisotropy ratios (including, specifically, an isotropic medium), the transmembrane current at any point depends on the second derivative of transmembrane potential in each coordinate direction evaluated at that point. This result is a generalization of the one-dimensional cable equation where the transmembrane current per unit length, i_m, is (14)

$$i_m = g_i\, \partial^2 V_m/\partial x^2 \tag{22}$$

and g_i is the intracellular conductance times length (unbounded medium).

If Eq. 21 is substituted into Eqs. 4 and 5 then, by inspection, one has

$$\Phi_o = -\left(\frac{1}{1 + \lambda}\right) V_m \tag{23}$$

$$\Phi_i = \left(\frac{\lambda}{1 + \lambda}\right) V_m. \tag{24}$$

These equations are generalizations of the one-dimensional cable relationships as noted, for example, by Hodgkin and Rushton (14). In particular the intracellular current density $\bar{J}_i$ and interstitial current density $\bar{J}_o$, using Eqs. 23 and 24 in Eqs. 1 and 2 satisfy

$$\bar{J}_i = -\bar{J}_o \tag{25}$$

just as in cable theory.

Evaluation of I_v for General Anisotropy Ratios

The similarities between one-dimensional cable theory and two-dimensional behavior arise solely for isotropic media or for anisotropic media with equal anisotropy ratios. The conductivity measurements of Clerc (1) and Roberts et al. (5, 6) agree to the extent that all clearly indicate that cardiac tissue does not satisfy the equal anisotropy condition. As a consequence we were led to explore the particular current patterns arising in several specific examples by numerical evaluation of Eqs. 11 and 17.

Eq. 17 can be interpreted as evaluating the transmembrane current density at a site (x, y) through the convolution of a source function $S(x', y')$, where

$$S(x', y') = g_{ox}\partial^2 V_m/\partial x'^2 + g_{oy}\partial^2 V_m/\partial y'^2 \tag{26}$$

with the weighting function

$$w(x - x', y - y') = \frac{\lambda_x - \lambda_y}{2\pi G(1 + \lambda_x)(1 + \lambda_y)} \left\{ \frac{\dfrac{(x - x')^2}{G_x} - \dfrac{(y - y')^2}{G_y}}{\left[\dfrac{(x - x')^2}{G_x} + \dfrac{(y - y')^2}{G_y}\right]^2} \right\}. \tag{27}$$

Except when $\lambda_x = \lambda_y$ and w is a two-dimensional delta function, $I_v(x, y)$ will depend on $S(x', y')$ at distant points as well as in the neighborhood of x, y. A measure of the extent of the region influencing $I_v(x, y)$ is contained in the "shape" of the weighting function. If we make a simple scale transformation of

$$X = x/(G_x)^{1/2} \qquad Y = y/(G_y)^{1/2} \tag{28}$$

then

$$w(X - X', Y - Y') = \frac{\lambda_x - \lambda_y}{2\pi G(1 + \lambda_x)(1 + \lambda_y)} \left\{ \frac{[(X - X')^2 - (Y - Y')^2]^2}{[(X - X')^2 + (Y - Y')^2]^2} \right\}. \tag{29}$$

In this coordinate system, the weighting function has a particularly simple form in polar coordinates. We obtain this by first choosing, for simplicity, $x = y = 0$ (i.e., the field point is at the origin) and defining $r = (X'^2 + Y'^2)^{1/2}$ and $\theta = \arctan(Y'/X')$. Then Eq. 29 becomes

$$w(X', Y') = w(r, \theta) = \frac{\lambda_x - \lambda_y}{2\pi G(1 + \lambda_x)(1 + \lambda_y)} \cdot \frac{\cos 2\theta}{r^2}. \tag{30}$$

The magnitude falloff as $1/r^2$ clearly emphasizes the contribution to $I_v(x, y)$ from the neighboring source region. In fact, in the numerical evaluation of Eq. 17 it is convenient to separate out the local region (which is treated by actually evaluating the integral) and the more distant regions that can be approximated by discretization of the integral. In the simulations to be presented we will discuss the relative contributions that might arise from near, intermediate, and distant terms.

Longitudinal Currents

In the previous section we emphasized the derivation and behavior of an expression for transmembrane current in anisotropic tissue for two reasons. First, this relationship is not a simple extension of one-dimensional cable theory. Second, such an expression is essential to simulation of activation of such tissue assuming the applicability of some Hodgkin-Huxley type membrane model that provides a relationship between transmembrane ionic current and transmembrane potential and time. In setting up such a simulation one must equate the ionic and capacitive current to an expression such as Eq. 17.

Using the best available conductivity data of Clerc (1) shows that, indeed Eq. 25 is not satisfied and $|\bar{J}_i| \neq |\bar{J}_o|$. As a means of highlighting the behavior of current flow in anisotropic tissue that differs from that in isotropic tissue (or tissue with equal anisotropy) we define "difference currents" (actually the difference of absolute magnitudes) as

$$I_{dx} = I_{ox} + I_{ix} \tag{31}$$

and

$$I_{dy} = I_{oy} + I_{iy} \tag{32}$$

(where I_{ox}, I_{oy} are interstitial and I_{ix}, I_{iy} intracellular longitudinal components). The current $\bar{I}_d = (I_{dx}\,\bar{a}_x + I_{dy}\,\bar{a}_y)$ is zero for isotropic and equal

anisotropic conductivity ratios, and serves as a quantitative measure of the degree of deviation from simple core conductor type behavior. By virtue of Eq. 3 $\bar{I}_d$ is solenoidal.

NUMERICAL MODEL

In this paper our goal is to examine the current distribution produced in tissues with three sets of conductivities, due to the same, fixed-source configuration (circular isochrone). Specifically, we wish to calculate longitudinal currents $\bar{J}_i$ and $\bar{J}_o$, transmembrane currents, and composite-current flow maps for varying conductivities to see how the results compare with the traditional one-dimensional picture of equal and opposite intra- and extracellular current flow, which are almost entirely limited to the rising phase, or activation, zone.

Tissue Conductivities in the Simulations

The three examples are called "isotropic," "nominal," and "reciprocal." We chose one to be isotropic both as a contrast with the two examples of anisotropicity and as a means for evaluating the accuracy of numerical procedures since analytic relationships arise for this case. A second set of tissue conductivities was chosen to correspond to some measured values of conductivity (the "nominal" case). A third tissue example was defined in such a way that interstitial conductivity parameters were reciprocal of intracellular ones. This "reciprocal" case is an exaggeration of realistic tissue and more readily demonstrates phenomena that are less apparent in the latter case. The actual values of the conductivities chosen and the conductivities measured by Clerc (1) and by Roberts and co-workers (5, 6) (which constitute the only published data) are shown in Table I.

Analytic Expression for Transmembrane Potential (V_m)

The voltage across the membrane at any point x, y, i.e., $V_m(x, y)$, was chosen as (15)

$$V_m = 52 \tanh [5.4(R_u - R)] - 38 \qquad (33)$$

where $R_u = 2$, $R = (x^2 + p^2y^2)^{1/2}$, $p^2 = \Theta_x^2/\Theta_y^2$, and Θ_x, Θ_y are the velocity along x and y of the isochrones. Among the considerations involved in the choice of this function were (*a*) its shape is approximately that of a real action potential, (*b*) it has analytic first and second derivatives, and (*c*) it decays exponentially into resting and plateau voltages on the leading and trailing edges. Constants 52, 5.4, and −38 were chosen to give the action potential a peak-to-peak height of 104 mV, a width of ~1 mm, and a resting potential of −90 mV. For Eq. 33, p was made equal to 1 for the circular isochrone and 2 for the elliptical isochrone. Eq. 33 assumes the propagation velocity along any radius to be a constant and the temporal action potential to be the same everywhere. The derivatives of V_m and the nomenclature used are described in Appendix A.

The assumption of a fixed morphology for the rising phase of the action potential can be justified in the case of a continuous media according to the Hodgkin-Huxley formulation. Clerc (1) postulated that this condition would also be satisfied in the case of cardiac tissue and cited experimental verification. But more careful study by Spach (16) has shown this to be only a rough approximation and that a consistent change in morphology does result from changes in load (i.e., change in direction of propagation relative to fiber axis). Using V_{max} as a measure of the rising phase waveform, Spach (16) describes an experimental variation of 124 to 171 V/s (15% variation from the mean). While this is a significant change, it is a modest one, so that the assumption of a fixed waveform should be satisfactory as a first approximation. One can examine the temporal action potential in the plane of collision of two linearly propagating waves (where the axial impedance is necessarily infinite) to see that the rising phase is not greatly different from that elsewhere. The experiments of Spach et al. (17) and Ushiyana (18) show that the range of variation that can be expected is modest.

Numerical Integrations

Calculation of the currents for each set of conductivities primarily involved achieving accurate numerical evaluation of combinations of Eqs. 1–32. In many cases, the principal step is approximating an (analytic) integration by a numerical summation. Performing the numerical integrations involved (*a*) selecting the field points (points for which results were to be calculated), and (*b*) conceptually subdividing the surface of the tissue into a grid of elemental areas. The difficulty in the latter step is providing a subdivision small enough to take into account the rapid change with distance of such functions as the second derivatives of V_m without making the overall calculation excessively long or unduly sensitive to the accumulation of round-off errors.

Organization of the Tissue Geometry

For the purpose of making the aforementioned numerical calculations, we considered a square block of tissue 8 mm on a side. The source was a concentric circular isochrone, with radius of 2 mm along which V_m was halfway between its resting and plateau values (chosen to be −90 and 14 mV, respectively). Because the spatial distance over which V_m varies is ~1 mm (over this distance the voltage changes from −89.5 to 13.5 mV), the 4-mm distance from the center to the edge provided ~2 mm or two excitation wave thicknesses ahead of and behind the wavefront.

Calculations required both the location of particular points on the surface of the tissue and integration over the surface. To facilitate these calculations, the 8-mm square block of tissue was thought of as having superimposed on it a grid of points, called "nodes," separated by a distance dx (dy) along axis x (y). These distances were usually 0.1 mm. With one node at the center, there were then 40 nodes along the positive x axis and 81 nodes in all along x, and similarly for y. Field points for all calculations were chosen as some subset (or all) of these nodes (81 × 81 = 6,561 in all).

Numerical integrations over the surface of the tissue made use of the squares into which the nodes divided the surface. We considered a "major square" to be one with a node at each of its four corners. Note that nodes

TABLE I
CONDUCTIVITY VALUES

S/mm	Clerc*	Roberts‡	Roberts§	Nominal	Isotropic	Reciprocal
g_{ix}	1.74×10^{-4}	2.78×10^{-4}	3.44×10^{-4}	2×10^{-4}	1×10^{-4}	2×10^{-4}
g_{iy}	1.93×10^{-5}	2.63×10^{-5}	5.96×10^{-5}	2×10^{-5}	1×10^{-4}	2×10^{-5}
g_{ox}	6.25×10^{-4}	2.22×10^{-4}	1.17×10^{-4}	8×10^{-4}	1×10^{-4}	2×10^{-5}
g_{oy}	2.36×10^{-4}	1.33×10^{-4}	8.02×10^{-5}	2×10^{-4}	1×10^{-4}	2×10^{-4}

*Measured data expressed by Clerc (1) as a specific resistivity in the restricted intracellular or interstitial space. It was converted to the values listed above by using the ratio (intracellular space)/(interstitial space) = 0.7/0.3, as was used by Clerc.
‡Data from Roberts et al. (5).
§Data from Roberts and Scher (6).

were not at the centers of major squares. Functions were not assumed constant over a major square (indeed most were not); rather, major squares were dynamically subdivided into smaller ones as described below. The number of major squares usually was 80 by 80, or 6,400 in all.

In concept, our interest was in performing calculations for two-dimensional tissue of infinite extent. No significant limitation to this concept was caused by our restricting the size of the tissue block to an 8-mm square since all the results depended, among other things, on multiplication by derivatives of V_m, and these values were insignificantly different from zero outside the tissue block. Conversely, since our interest was in the results for infinite extent, no effect of a boundary along x or y was included (or necessary).

Therefore, the purposes of defining the 8-mm square tissue block were (*a*) to define a region where all nonzero values of derivatives of V_m would be found, and (*b*) to define on the region a collection of nodes to be used as field points, and hence provide us with a particular set of points where values of different potentials or currents could be compared. However, these nodes were not the only points at which functions could be or were evaluated in the course of numerical integrations.

Grid Subdivision. To perform numerical integrations over the surface of the tissue, the surface was subdivided (dynamically) in such a way that the variation in function *V2*, Eq. A6, did not exceed a limit. The limit was chosen as

$$DEL = \text{limit of allowed variation in } V2 = PC \times V2\text{MAX} \tag{34}$$

where $V2\text{MAX} = \max |V2|$ over all the nodes in the grid, and where $PC = 0.25$ in most calculations. Since function *V2* depended on the second derivatives of V_m and therefore varied rapidly from node to node, it was to be expected that no node would fall precisely on the maximum *V2* value; however, we considered this fact unimportant since *PC* was as large as 0.25 and *DEL* was therefore not a precise (sharp) limit on variations in *V2* as much as a boundary limiting gross changes. The subdivision was based on function *V2*, which appears in the integration for Φ and other field quantities, because as a combination of the weighted x and y second derivatives of V_m, it changes more rapidly than V_m or its first derivatives. Hence, our assumption was that a subdivision small enough for *V2* also would be adequate for functions of V_m or its first derivatives. Details of the dynamic subdivision procedure are given in Appendix B.

Evaluation of Currents and Potentials

In the evaluation of Φ_i from Eq. 11, the variation in the log function was assumed to be small over an elemental square and well-represented as a constant at the value taken on at the center of the square. This assumption is most severely tested in squares that touch the field point, where the log function is singular. A comparison of the approximate solution with a rigorous solution (assuming the source function to be constant) shows the error to be under 6% for the nominal conductivity parameters and under 3% for reciprocal anisotropy tissue.

The evaluation of Eq. 17, numerically, poses an additional problem because of the higher-order singularity of the weighting function. This is dealt with by assuming that the source function is constant over the elemental squares that touch (i.e., are nearest to) the field point. This results in a "self term" that can be evaluated by actually integrating the weighting function. The accuracy of the procedure can be enhanced by using the nesting procedure described earlier, in which case only those squares actually touching the field point are evaluated from the self-term formula while remaining integration elements are determined by assuming the integrand to be constant at the value taken at the center of the square.

To integrate Eq. 17 over a small square centered on the field point, the strategy is first to transform the differential operator to the Laplacian, then to use the divergence theorem to convert the surface integral into a line integral. Because the integrand is well behaved over the square contour, the singularity difficulty is avoided. Details of this procedure are given in Appendix C.

The numerical evaluation of I_v was split into three terms. The immediate surrounding square was evaluated from "self-term" expression (Eq. C4). A "near-region" term was evaluated by discretization of Eq. 17 as applied to the 0.2-mm square surrounding the field point, but excluding the self-term square. The remaining region contributed to the "distant term." Details of this procedure are given in Appendix D. For the nominal case the contributions of each of the above described component terms to the transmembrane current is given in Table II for field points along the x axis (for the circular isochrone centered at $r = 2$ mm). One notes that even near the peak values of I_v the contribution from the near and distant terms is not negligible. For regions where I_v is small, it is not surprising, of course, to note that the major contribution comes from distant terms (where the source strength is larger).

I_v can be estimated from Φ_i using Eq. 4 and second differences. Designating the quantity so derived as $[I_v]_\Phi$ we have, specifically,

$$[I_v]_\Phi = g_{ix} \cdot \{[\Phi_i(x + \Delta, y) - 2\Phi_i(x, y) + \Phi_i(x - \Delta, y)]/\Delta^2\} + g_{iy} \cdot \{[\Phi_i(x, y + \Delta) - 2\Phi_i(x, y) + \Phi_i(x, y - \Delta)]/\Delta^2\}. \tag{35}$$

Accuracy of evaluation of Eq. 35 depends importantly both on the accuracy of Φ_i and choice of incremental distance Δ. Mathematically, the numerical difference, if exact, more closely approximates the desired derivative as Δ becomes smaller; conversely, numerical inaccuracies in computing Φ_i make second differences in Φ_i increasingly inaccurate as Δ becomes small enough that the most significant digits in Φ_i are simply subtracted. Trial and error evaluation of Eq. 35 showed that with Δ chosen smaller than 0.1 mm the computed membrane current became noisier rather than more accurate; therefore, Δ of 0.1 mm was used. Actual calculation of each of the five values of Φ_i appearing in Eq. 35 was by means of the CPHI11 subroutine (described in Appendix E), the same procedure used in simply tabulating values of Φ_i itself.

Table II contains the transmembrane current found from Eq. 35 that can be compared with that derived from Eq. 17; the two are sufficiently similar to confirm internal consistency. Nevertheless, the numerical noise introduced in the evaluation of the second derivative is evident as well, and supports the use of Eq. 17 for accurate evaluation of I_v.

In the case of equal anisotropy one can examine the computed Φ_i to determine whether Eq. 24 is satisfied. For an elliptical isochrone with $\lambda = 4$, Fig. 1 shows the variation of 0.8 V_m along the major axis of the ellipse and the value of $(\Phi_i + 19.8)$ (where Φ_i is translated for ease of comparison) using the value of Φ_i as derived from Eq. 11. These curves should be identical, according to Eq. 24, and one can see that the agreement is quite satisfactory. As with transmembrane current the longitudinal currents can be derived from Φ_i (and $\Phi_o = \Phi_i - V_m$) by numerically estimating derivatives. However, greater accuracy can be obtained by deriving expressions directly; details are given in Appendix F. While $\bar{I}_d$ can be found from Eqs. 31 and 32, one again finds that greater accuracy is obtained by deriving fresh expressions for the desired field. In this case, in particular, a nearly isotropic tissue will contribute nearly cancelling values to Eqs. 31 and 32, magnifying small errors. The derived expressions are provided in Appendix F.

RESULTS

A description of the program organization for calculating intra- and extracellular potentials, longitudinal and transmembrane currents, for each of the three types of tissue conductivities being examined is given in Appendix E. The longitudinal intracellular and interstitial current flow patterns (plus associated transmembrane currents) are shown in Figs. 2–7. To help explain these Figures, Fig. 2 shows

TABLE II
COMPONENT CONTRIBUTIONS TO TRANSMEMBRANE CURRENT: NOMINAL CONDUCTIVITY CASE

X coordinate of field-point ($y = 0$)	$[I_v]_\Phi$	I_v(total)	I_v(self)	I_v(near)	I_v(distant)
0.2	-1.1×10^{-4}	-5.0×10^{-5}	-6.6×10^{-8}	-1.9×10^{-10}	-5.0×10^{-5}
0.4	7.5×10^{-4}	-5.4×10^{-5}	-5.4×10^{-8}	-1.2×10^{-9}	-5.4×10^{-5}
0.6	-8.0×10^{-4}	-6.0×10^{-5}	-4.6×10^{-7}	-8.7×10^{-9}	-6.0×10^{-5}
0.8	1.0×10^{-3}	-7.2×10^{-5}	-4.0×10^{-6}	-6.9×10^{-8}	-6.7×10^{-5}
1.0	5.6×10^{-4}	-1.2×10^{-4}	-3.4×10^{-5}	-5.6×10^{-7}	-8.0×10^{-5}
1.2	-5.0×10^{-4}	-4.6×10^{-4}	-3.0×10^{-4}	-4.6×10^{-6}	-1.6×10^{-4}
1.4	-4.9×10^{-3}	-3.5×10^{-3}	-2.6×10^{-3}	-4.0×10^{-5}	-8.7×10^{-4}
1.6	-2.97×10^{-2}	-2.61×10^{-2}	-2.11×10^{-2}	-4.20×10^{-4}	-4.66×10^{-3}
1.8	-1.28×10^{-1}	-1.48×10^{-1}	-1.23×10^{-1}	-5.70×10^{-3}	-1.95×10^{-2}
2.0	-3.39×10^{-3}	-2.82×10^{-3}	-4.76×10^{-3}	1.24×10^{-4}	1.82×10^{-3}
2.2	1.26×10^{-1}	1.47×10^{-1}	1.19×10^{-1}	5.35×10^{-3}	2.20×10^{-2}
2.4	2.91×10^{-2}	2.58×10^{-2}	2.06×10^{-2}	3.14×10^{-4}	4.93×10^{-3}

Relative contribution to the total transmembrane current evaluated from Eq. 17 from the "self-term" "near term," and "distant term" defined in text and further described in Appendix D. $[I_v]_\Phi$ is the transmembrane current found from an evaluation of Φ_i utilizing a numerical evaluation of Eq. 4.

the 0.5-mm-square grid structure of the upper-right quadrant of the 8 mm × 8 mm tissue preparation. The total intracellular, interstitial, or "difference" current crossing each 0.5-mm grid element was evaluated and represented by line density in the current flow figures. Because current lies in two superimposed domains, linked by transmembrane current, we distinguish the interstitial from the intracellular components by dashed or dotted lines, respectively. Where equal and opposite such currents exist, some simplification in the figures has been accomplished by showing only the intracellular current but using a solid line signifying that an interstitial current in the opposite direction is also present. Transmembrane current is indicated by a large dot (suggesting current emerging into the interstitial space from intracellular) or a large cross (with the reverse connotation).

The flow pattern was based on currents crossing the sides of 0.5-mm square. While resolution would be improved for smaller squares, it was felt that the increased demand on graphical display would add an unnecessary complexity. However, the reader must bear in mind that the present scheme reflects spatial and amplitude quantization error.

Some appreciation of this artifact is evident in Fig. 2, which is the pattern arising from a circular isochrone lying in an isotropic tissue (the isochrone geometry is also shown in Fig. 2). The intracellular current should be radial and outward and of constant magnitude on a fixed radius. This behavior is reflected only crudely since the 0.5-mm grid is

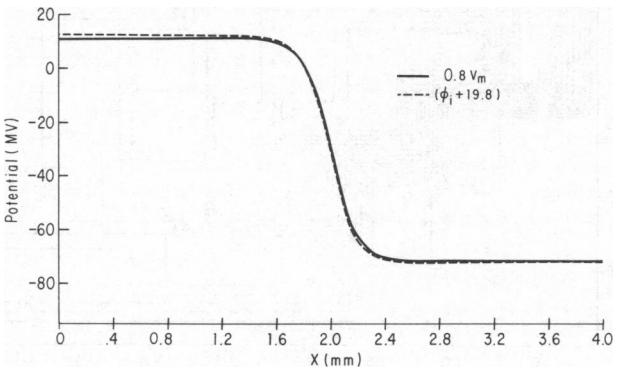

FIGURE 1 A comparison of the intracellular potential evaluated numerically with that obtained directly from an analytic expression. The source is represented by an elliptical isochrone, with major axis to minor axis ratio of 2, in a two-dimensional medium of equal anisotropicity ratio ($\lambda = 4$). The transmembrane potential is described by Eq. 33.

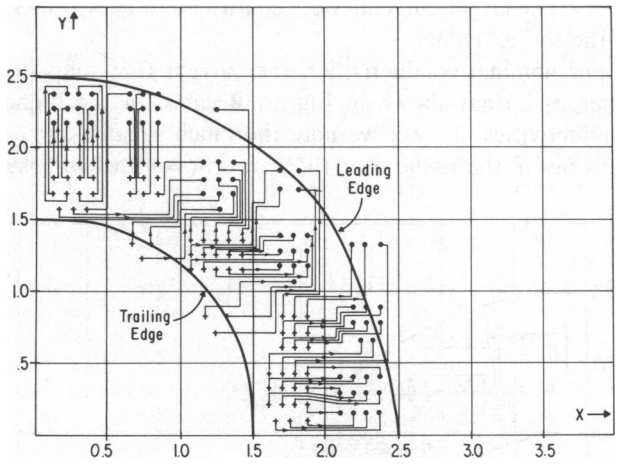

FIGURE 2 *Isotropic* ($g_{ix} = g_{iy} = g_{ox} = g_{oy} = 1 \times 10^{-4}$ S/mm): The upper right quadrant of an 8 mm × 8 mm tissue slice is shown. The basic grid is square with points separated by 0.5 mm. The active region is essentially delimited by the circular leading and trailing edge within which the transmembrane potential varies from resting to plateau condition (described mathematically by Eq. 33). The behavior is assumed to be two dimensional. The intracellular current flow field for an isotropic media is shown which correctly describes the net current crossing any 0.5 mm segment according to the scale of 5,000 (relative) units per current line. Corresponding to each intracellular current line is an interstitial current line in the opposite direction (not shown). Large dots reflect outward transmembrane current (from intracellular to interstitial) while large crosses represent inward transmembrane current, with the scale of 5,000 current units per element (dot or cross) per unit square.

not much smaller than the excitation wave width of ~1 mm.

Because the total current (or the difference current) must be solenoidal, closed paths should be seen in Figs. 2–4, and 6, except for current leaving at the top or right (which flows into regions of the tissue beyond that represented by the figure). The total outflow should equal the total inflow, a property that serves to check the accuracy of the simulation. Errors were generally below 10% and usually below 5%. However, because the amplitude quantization, current entering a square with a magnitude large enough to justify representation by a current line can divide into two or three parts, all of which are "below threshold"; it is this artifact that primarily accounts for the several starts or stops that can be seen in these figures.

The isotropic case is included also as a reference for the subsequent plots since this simulation, which basically conforms to expectations derived from the one-dimensional continuous cable, is relatively familiar. In particular, one confirms that $I_{ix} = -I_{ox}$ and $I_{iy} = -I_{oy}$. Furthermore, except for the artifact introduced by spatial quantization, the total longitudinal current is in fact radial and of equal magnitude along any radius (e.g., trailing or leading edge isochrone). Similarly, the transmembrane current is the same along any fixed radius.

The longitudinal and transmembrane currents for this case can also be derived directly from the transmembrane potential (essentially from Eqs. 21, 23, 24, 1, and 2), and this serves as a valuable check on the numerical procedures. The larger currents were confirmed to be within 3% of the correct value.

For nominal conductivities, the current flow map that emerges is that shown in Fig. 3. Because of the higher conductivities along x we note the much greater current densities in the tissue near the x axis in contrast to tissue near the y axis. In the latter region in spite of the membrane tending to drive currents radially (i.e., in the y direction) the x component of current is not too much less than the y component.

While most of the interstitial current is equal and opposite to the intracellular current, significant differences arise. Such differences are distinguishing features of anisotropic tissue with unequal anisotropy ratios, as discussed earlier. These features are highlighted by plotting "difference" currents that are obtained from the difference in magnitude between interstitial and intracellular currents (actually the algebraic sum of intracellular and interstitial current). These are plotted in Fig. 4 for the nominal tissue.

In viewing the difference currents shown in Fig. 4, it should be noted that each line represents only one-tenth the value of each current line in Fig. 3. While nowhere near dominant, they are significant. Their shape conforms to the solenoidal expectation (aside from quantization artifact). Particularly noteworthy is the large extent of spread of these currents well beyond the region of local activation. Through reference to Fig. 3 (and the unquantized data) one notes that in the high-current density regions, vertical current magnitudes are greater interstitially while horizontal current magnitudes are greater intracellularly. This is what would be expected based on the relative interstitial-intracellular conductivity.

The reciprocal conductivity condition provides an exaggerated example where interstitial current is encouraged to flow mainly in the y direction and intracellular current flows mainly in the x direction. The result is the formation of closed current paths that cross the membrane several

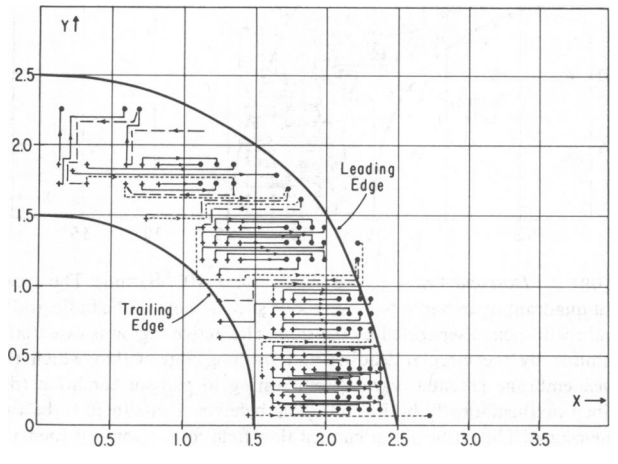

FIGURE 3 Nominal ($g_{ix} = 2 \times 10^{-4}$ S/mm, $g_{iy} = 2 \times 10^{-5}$, $g_{ox} = 8 \times 10^{-4}$, $g_{oy} = 2 \times 10^{-4}$). ●, outward transmembrane current, +, inward transmembrane current (____) intracellular current for which equal and opposite interstitial current is not shown. (----) longitudinal interstitial current (····) longitudinal intracellular current. Each line represents 10,000 (relative) units of current. Source field shown in Fig. 2.

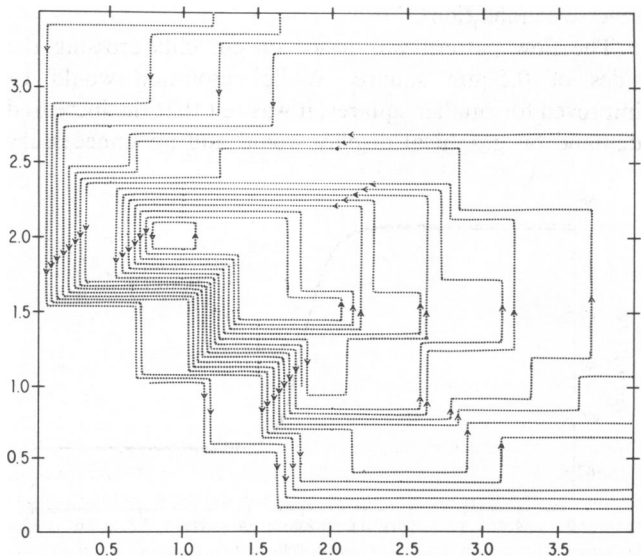

FIGURE 4 Difference current for nominal conductivities (see caption for Fig. 3), as defined in Eqs. 31 and 32. No assignment of the result to intracellular or interstitial path is made on the figure. Each line represents 1,000 (relative) units of current (compare with Fig. 3). Source field shown in Fig. 2.

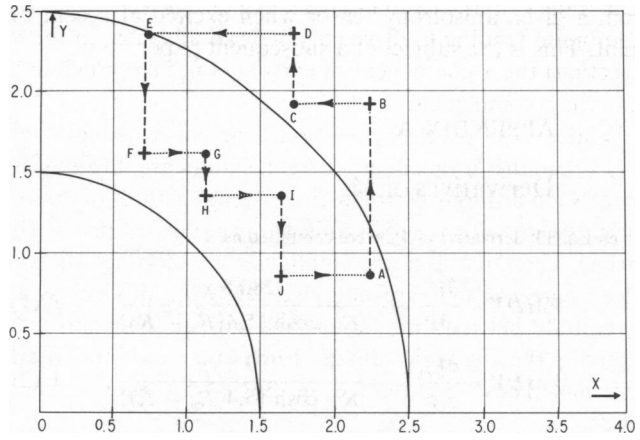

FIGURE 5 A closed current pathway for reciprocal anisotropy (see caption for Fig. 6). Membrane is crossed at *A, B, C, D, E, F, G, H, I, J*. ●, outward transmembrane current; +, inward transmembrane current; ----, longitudinal interstitial current; ····, longitudinal intracellular current. Source field shown in Fig. 2.

times to utilize these preferred directions, yet fulfill the requirement of a closed loop. One such pathway is shown in Fig. 5 while the more complete map from which it is derived is shown in Fig. 6. A full description of the current flow in the reciprocal conductivity bidomain is difficult because of its complexity, as exemplified above. For this reason, we've chosen to provide three figures describing the current field, no one of which is complete in all respects. In Fig. 6, all currents external to the active region are represented, but within the active region transmembrane currents are suppressed. Furthermore, within the active region, only a few longitudinal currents are given in detail; in most cases only the net current crossing the sides of the 0.5-mm squares is provided. One could, in fact, reconstruct all details, recognizing the continuity of current requirement. Fig. 7 provides much of the missing picture, since it gives a full description of the transmembrane current (alone). The separation into these components of the complete current field was necessary to keep any one figure from becoming excessively complicated.

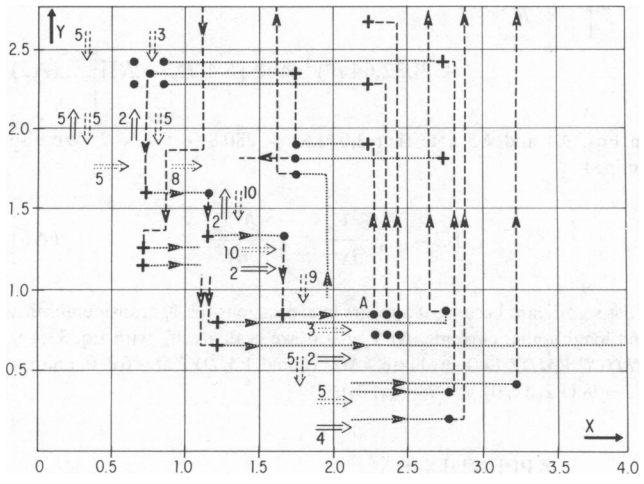

FIGURE 6 Current flow map for reciprocal anisotropy ($g_{ix} = 2 \times 10^{-4}$ S/mm, $g_{iy} = 2 \times 10^{-5}$, $g_{ox} = 2 \times 10^{-5}$, $g_{oy} = 2 \times 10^{-4}$). Intracellular, interstitial and transmembrane currents are shown. ●, outward transmembrane current; +, inward transmembrane current; ——, intracellular current for which equal and opposite interstitial current is not shown; ----, longitudinal interstitial currents; ····, longitudinal intracellular current. Large numbered arrows represent the (numbered) additional current (lines) crossing the respective square boundary. Transmembrane current in the active region shown only in part (see Fig. 7 for complete values). Each line represents 5,000 (relative) units of current. Source field shown in Fig. 2.

The loop identified in Fig. 5 has 10 membrane crossings and has a length of ~6 mm. It typifies loops of smaller or larger size with more or fewer membrane crossings that arise in the reciprocal conductivity example. It is clear that excitatory patterns arising from current loops of this kind must differ greatly from simple two-dimensional extensions of one-dimensional continuous cable theory (the latter being exemplified by the case of equal anisotropy ratios).

The pattern of transmembrane current is shown in Fig. 7. It is interesting that peripheral outward (depolarizing) current is clustered near the x axis while inward (hyperpolarizing) current clusters along the y axis. This distinction has clear implications for restructuring the isochrone shapes from the initial circular one.

While the reciprocal conductivity case is an exaggerated condition that does not arise in real cardiac tissue, it clearly reflects some aspects of the normal current field. The latter case can be viewed as having properties that lie somewhere between the isotropic and reciprocal case. In particular, one sees some of the spreading out of current, and some multiple crossing of the membrane as well as the obvious changes from symmetry in current magnitudes, as was noted earlier.

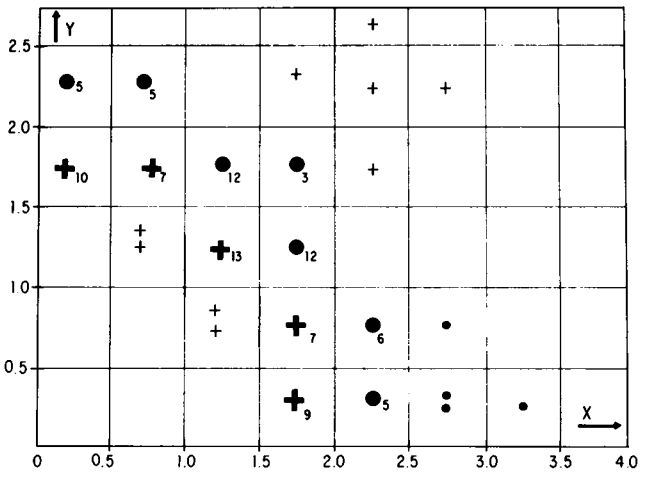

FIGURE 7 Transmembrane currents for reciprocal anisotropy (as in Fig. 6). Shown is the complete map of transmembrane current per square. ●, outward transmembrane current. +, inward transmembrane current. Numbers indicate the number of lines of current if three or greater. These details are associated with the map in Fig. 6. Each line represents 5,000 (relative) units of current. Source field shown in Fig. 2.

DISCUSSION

We have examined the currents and potentials arising in two-dimensional anisotropic cardiac tissue due to a circular-shaped isochrone action potential source. In addition to nominal tissue, isotropic and reciprocal anisotropy were chosen as representative, in an extreme way, of two component aspects of the normal case.

For isotropicity, two-dimensional behavior appears as a relatively straightforward generalization of one-dimensional continuous cable theory. In particular, longitudinal currents in intracellular space are equal and opposite that in interstitial space. Also transmembrane currents are derivable from spatial second derivatives of transmembrane potentials at the same position. These same conclusions also hold in the case of anisotropic tissue when the anisotropy ratios of intracellular and interstitial space are equal.

When the anisotropy ratios are unequal, the transmembrane current can be obtained from the second derivatives of the transmembrane potential only through a surface integration, though the second derivative source is strongest in the immediate vicinity of the field point. We have developed and demonstrated a successful numerical method of dynamic subdivision of the area to be integrated, which results in the greatest refinement of area elements in that region contributing the most.

This adaptive numerical technique has permitted carrying out in a reasonable computer time an examination of the current field in the reciprocal and nominal conductivity case. The reciprocal example illustrates most dramatically that the intracellular longitudinal current is not equal and opposite the interstitial. In fact, one can trace current loops that cover large distances and that involve multiple membrane crossings (these permit flow in a particular direction in a preferred space enjoying a high conductivity). The current flow takes on a staircase configuration in the vicinity of the source region. The form of these action currents strongly suggests that the isochrone will be reshaped. Possibly more importantly is the implication for greater tissue interactions with significance to the study of arrhythmias.

Normal tissue reflects both isotropic and reciprocal behavior. One sees to a large extent equal and opposite longitudinal currents. But in addition, as depicted on the difference maps, there are component current loops that range over larger distances and that may involve multiple membrane crossings. While of relatively diminished amplitude these could be significant. The behavior of diseased (e.g., ischemic) tissue is unexplored from this viewpoint.

The ability to calculate the transmembrane current from the distribution of transmembrane potential, even in tissue with arbitrary anisotropy, permits simulation of the activation patterns by a consideration of membrane properties with a Hodgkin-Huxley behavior. This permits an examination of the actual isochrone shape to be expected from a given anisotropy tensor when excited at a central point. This is the subject of a subsequent paper.

APPENDIX A

Derivatives of V_m

Given Eq. 33, derivative of V_m were computed as

$$VMDX = \frac{\partial V_m}{\partial x} = -\frac{280.8\,x}{R \cdot \cosh^2[5.4(R_u - R)]} \tag{A1}$$

$$VMDY = \frac{\partial V_m}{\partial y} = -\frac{280.8\,yp}{R \cdot \cosh^2[5.4(R_u - R)]}. \tag{A2}$$

In Eqs. A1 and A2, 280.8 = 52 × 5.4, and p = velocity x/ velocity y. To find the second derivatives, we defined

$$t_A = -\frac{1}{R \cdot \cosh^2[5.4(R_u - R)]} \tag{A3}$$

so that

$$VMDX2 = \frac{\partial^2 V_m}{\partial x^2}$$

$$= t_A\left(\frac{280.8\,p^2 \cdot y^2}{R} + 3{,}032.64\,x^2 \tanh[5.4(R_u - R)]\right) \tag{A4}$$

and

$$VMDY2 = \frac{\partial^2 V_m}{\partial y^2}$$

$$= t_A\left\{\frac{280.8\,p^2 \cdot x^2}{R} + 3032.64\,p^4y^2 \tanh\,[5.4(R_u - R)]\right\}. \tag{A5}$$

In Eqs. A4 and A5 note that 3,032.64 = 280.8 × 5.4 × 2. We also defined

$$V2 = g_{ox}\frac{\partial^2 V_m}{\partial x^2} + g_{oy}\frac{\partial^2 V_m}{\partial y^2}. \tag{A6}$$

$V2$ is significant because it appears in expressions for Φ_i, transmembrane, and longitudinal currents. At $x, y = 0$, we evaluate V_m with Eq. 33, set $VMDX$, $VMDY$ to 0, evaluate $VMDX2$ and $VMDY2$ at $\pm dx$, 0, and set $V2 = \frac{1}{2}\,[V2(dx, 0) + V2(-dx, 0)]$.

APPENDIX B

Dynamic Subdivision Procedures

The procedure used in the dynamic subdivision was first to examine the value of $V2$ at the corners of each major square (see Fig. 8). The first step was to calculate

$$V2\text{max} = \text{maximum absolute value of } V2 \text{ over corners } p = 1 \text{ to } 4$$

$$V2\text{min} = \text{minimum absolute value of } V2,\ p = 1 \text{ to } 4. \tag{B1}$$

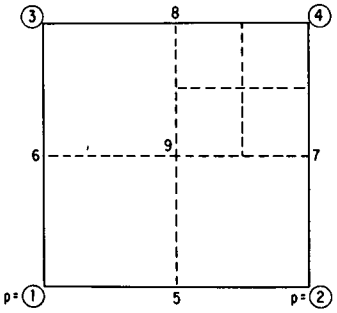

FIGURE 8 Subdivision of major squares. Encircled corners are numbers of corners of a major square and are connected by solid lines. Other numbers and dotted lines show the subdivisions that conditionally could occur.

Then,

$$\text{IF}\,|V2\max - V2\min| < DEL$$
$$\text{square 1-2-3-4 "was accepted"}$$
$$\text{ELSE square 1-2-3-4 "was subdivided."} \qquad \text{(B2)}$$

When a square "was accepted" then a counter, *LN*, first was incremented. Thereafter, the x, y coordinates of the square's center were determined from the x, y coordinates of corners 1–3, and a function *FCL* for the square was computed. The center coordinates and function were saved in list form

$$XCY(LN) = (x_1 + x_2)/2$$
$$YCL(LN) = (y_1 + y_3)/2$$
$$FCL(LN) = V2 \times DX \times DY / (4\pi G), \text{ where}$$
$$V2 = V2 \text{ at} XCL(LN), YCL(LN). \qquad \text{(B3)}$$

Note that although these lists contained elements originating on a two dimensional surface, Eq. (B3) contains only one-dimensional arrays, and, further, note that no explicit value was saved indicating the size of the element.

When a square "was subdivided," for example, square 1-2-3-4 was subdivided into four parts (Fig. 8), function *V2* was computed for each of the new points 5–9. In turn, the procedure above (Eqs. B1–B3) was repeated for squares 1-5-6-9, 6-9-3-8, 5-2-9-7, and 9-7-8-4. Any of these four squares were then either accepted or further subdivided; the figure indicates a further subdivision for square 9-7-8-4.

In discussing the subdivision, the original major square was said to be at level 1, the first subdivision of it at level 2, etc. In our programs we allowed dynamic subdivision down to level 6. Note that each level corresponds to an edge length

$$\text{edge length} = dx/2^{\text{level-1}} \qquad \text{(B4)}$$

so that level 6 subdivison corresponded to an edge length of <3 μm for a major square edge of 100 μm (0.1 mm). In fact, meeting Eq. B2 did not require this degree of subdivision when $PC = 0.25$. By this procedure, we subdivided the overall tissue block (Fig. 9). The results of the subdivision process for three cases, both in terms of the total number of squares into which the surface was subdivided and the number of different sizes, are shown in Table III.

Comments on Subdivision Criterion. While we wanted function *V2* to be constant over each square, each increase in the total number of squares brought with it a proportionate increase in the time required for every numerical integration, as well as the storage required for lists XCL, YCL, and FCL. Using the criterion of 25% of the maximum absolute value of *V2* obviously was a compromise. Because the limit *DEL* was derived from the maximum of *V2* anywhere on the grid, many squares not in the portions of the grid where V_m changed most rapidly were accepted without further subdivision, even though the percentage variation of V_m around the corners of that square was large. These squares were accepted without subdivision, since *V2* at all corners was small in comparison with the maximum absolute *V2* value, which was located elsewhere. Conversely, those squares in regions where there were the most rapid changes were subdivided extensively, with large numbers of squares at level 4 (12.5 μm), a desirable result. Because increasing the precision of calculation would be desirable in principle, one approach would be to decrease *PC* to a smaller value. However, empirical observation showed that a decrease to $PC = 0.125$ increased the number of squares by as much as a factor of 4, so we did not choose this alternative for these program executions.

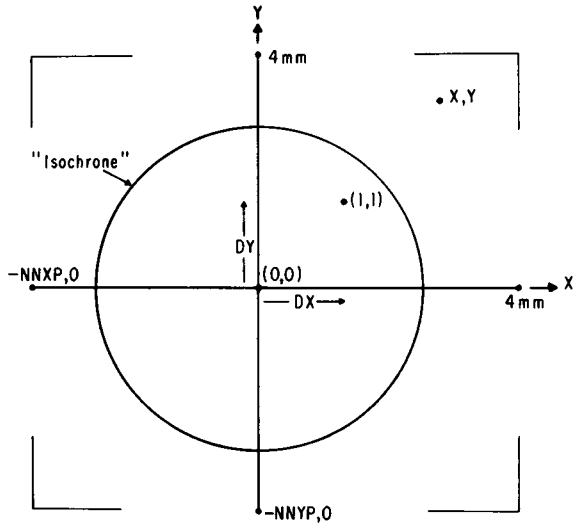

FIGURE 9 Overall dimensions of tissue block used for calculations (not drawn to scale). The parameter values given are those most frequently used. *NNXP* (*NNYP*) number of nodes along the X axis (Y axis) with positive x (y) coordinates.

Although the criterion was a compromise, the final number of squares used for the numerical integrations was 2–5 times larger than the 6,400 major squares. The efficiency of the dynamic subdivision method can be seen by realizing that uniform subdivision of the 8-mm^2 tissue block at 12.5 μm, the smallest size square actually used, would have required 4,096,000 squares.

TABLE III
RESULTS OF DYNAMIC SUBDIVISION PROCESS

Number of squares in subdivided grid	Isotropic	Nominal	Reciprocal
Total	20,860	14,200	13,324
Level 1 (100 μm)	5,588	5,856	5,940
Level 2 (50 μm)	1,768	1,388	1,144
Level 3 (25 μm)	3,392	1,884	1,632
Level 4 (12.5 μm)	10,112	5,072	4,608
Level 5	0	0	0
Tolerance DEL	3.17×10^{-2}	2.32×10^{-1}	5.71×10^{-2}

The total number of squares in the major grid is 6,400, with $dx = dy = 0.1$ mm. All entries used postulated a distribution for V_m with a circular equipotential at -38 mV at $R = 2$ mm. All executions allowed subdivision to level 6. No squares were used at levels 5 or 6 because the required condition was met by level 4.

APPENDIX C

Self Term Evaluation for Eq. 17

The appropriate linear transformation is given in Eq. 19 and leads to

$$I_v = \frac{(g_{ix}g_{iy})^{1/2}}{4\pi G}\,[g_{ox}\partial^2 V_m/\partial x'^2 + g_{oy}\partial^2 V_m/\partial y'^2]_{x'=y'=0} \int \nabla\cdot\nabla\left[\log\left(\frac{X'^2}{G_x/g_{ix}} + \frac{Y'^2}{G_y/g_{iy}}\right)\right] dx'dy' \quad (C1)$$

where the field point, for simplicity, was chosen as (0, 0), and the source function has been removed from the integral evaluated at the origin. Calling the coefficient of the integral F, and converting to a line integral by application of the divergence theorem, yields

$$I_v = F\int \frac{\dfrac{2X'\,\bar{a}_x}{G_x/g_{ix}} + \dfrac{2Y'\,\bar{a}_y}{G_y/g_{iy}}}{\left[\dfrac{X'^2}{G_x/g_{ix}} + \dfrac{Y'^2}{G_y/g_{iy}}\right]}\cdot\bar{n}\,dL' \quad (C2)$$

where the gradient operation has been performed. In Eq. C2 $\bar{a}_X$, $\bar{a}_Y$ are unit vectors in the X and Y directions, $\bar{n}$ is the unit vector normal to the contour and dL' is an element of contour. The integration over a square contour leads to standard integral expressions. The result turns out to be independent of the actual size of the square (though the approximation that the source function can be assumed constant implies that the square be small) and is

$$I_v = (2/\pi)[g_{ox}\partial^2 V_m/\partial x'^2 + g_{oy}\partial^2 V_m/\partial y'^2]\left[\frac{(G_y/g_{iy})^{1/2}}{(G_x/g_{ix})^{1/2}}\tan^{-1}\frac{(G_x/g_{ix})^{1/2}}{(G_y/g_{iy})^{1/2}} + \frac{(G_x/g_{ix})^{1/2}}{(G_y/g_{iy})^{1/2}}\tan^{-1}\frac{(G_y/g_{iy})^{1/2}}{(G_x/g_{ix})^{1/2}}\right]. \quad (C3)$$

This can be simplified a bit leading to

$$I_v = [g_{ox}\partial^2 V_m/\partial x'^2 + g_{oy}\partial^2 V_m/\partial y'^2]\cdot\left[\frac{g_{iy}}{G_y} + \frac{2(\lambda_y-\lambda_x)}{\pi(1+\lambda_x)(1+\lambda_y)}\tan^{-1}\left(\frac{G_x}{G_y}\right)^{1/2}\right]. \quad (C4)$$

Note that when $\lambda_y = \lambda_x$ (equal anisotropy ratio condition) Eq. C4 reduces to Eq. 21.

APPENDIX D

Calculation of Membrane Current From Transmembrane Voltage

Two different calculation procedures were used. The first was used when $|\lambda_x - \lambda_y| < (\lambda_x + \lambda_y)/100$, i.e., with equal anisotropy ratios (allowing a small numerical error). In this case,

$$I_V(x, y) = V2(x, y)/(1 + \lambda_x). \quad (D1)$$

In Eq. D.1, $V2$ is the function defined in Eq. A6.

The second procedure was the general case, and was used whenever the condition for equal anisotropy was not met. In the second case, the calculation was divided into three parts. An initial part was for the self term taken from Eq. C4 and applied to the immediate square region (see Fig. 10)

$$I_{V0}(x, y) = V2(x, y)\cdot g_{iy}/G_y - V2(x, y)\cdot\left\{\frac{\tan^{-1}[dy/dx\cdot(Gx/Gy)^{1/2}]}{\pi}\times\frac{2(\lambda_x-\lambda_y)}{(1+\lambda_x)(1+\lambda_y)}\right\} \quad (D2)$$

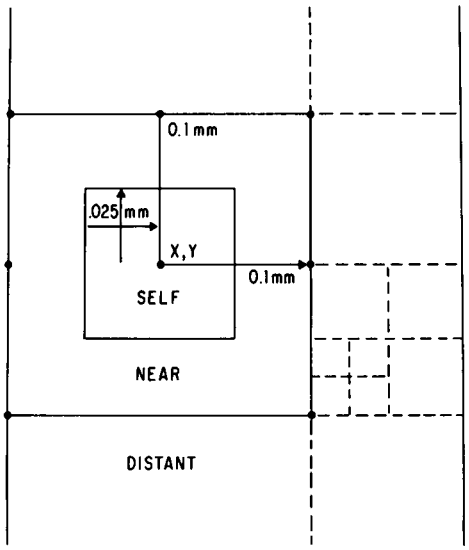

FIGURE 10 Division of surface into Self, Near, and Distant regions for computing I_V. The self region was the square with edges of 0.5 mm centered on the field point at x, y. The near region (not drawn to scale) was the square 0.2 mm on a side centered at x, y excluding the self region. The near region was divided into squares 0.25 mm on a side, and there were 60 of these. The distant region was all the rest of the surface, indicated here only schematically. Note that squares of varying size might border on the near region because of the dynamic subdivision algorithm. However, the corners of the near region had to be nodes.

where our calculations always had $dy/dx = 1$. Another part of I_V was

$$I_{V1}(x, y) = \frac{1}{4\pi G}\sum_{x'}\sum_{y'}\frac{\left\{\dfrac{(x'-x)^2}{G_x} - \dfrac{(y'-y)^2}{G_y}\right\}}{\left[\dfrac{(x'-x)^2}{G_x} + \dfrac{(y'-y)^2}{G_y}\right]^2} V2(x', y')\Delta x'\Delta y'\,\frac{2(\lambda_x-\lambda_y)}{(1+\lambda_x)(1+\lambda_y)} \quad (D3)$$

where the summation was over the near region. The near region was defined as that part of the surface within 0.1 mm of field point x, y along x or y, (Fig. 10), excluding those squares with a corner touching x, y. (Those squares accounted for the self term.) The near region was divided into squares with Δx, Δy = 0.25 mm, so there were 64 − 4 = 60 squares within it. Coordinates x', y' in the summations of Eq. D3 were the center of each of these near region squares, and $V2$ was evaluated at each one. This special subdivision of the region near each field point was used instead of the dynamic subdivision discussed in Appendix B because of the strong effect of the weighting function near the field point.

The final part of I_V involved evaluating Eq. D3 but in the distant region (Fig. 10). In this region, the previously tabulated function values (see Appendix E) could be used:

$$I_{V2}(x, y) = \sum_{LN=1}^{LT}\delta\cdot FCL(LN)\cdot\frac{\left(\dfrac{XD^2}{G_x} - \dfrac{YD^2}{G_y}\right)}{\left(\dfrac{XD^2}{G_x} + \dfrac{YD^2}{G_y}\right)^2}\cdot\frac{2(\lambda_x-\lambda_y)}{(1+\lambda_x)(1+\lambda_y)} \quad (D4)$$

where

$$\delta = 1 \text{ when } |XCL(LN) - x| > 0.1 \text{ mm}$$
$$\text{or } |YCL(LN) - y| > 0.1 \text{ mm}$$
$$\delta = 0 \text{ otherwise (square in near or self region)}$$
$$XD = XCL(LN) - X,\ YD = YCL(LN) - Y.$$

Note that a straightforward condition was applied to exclude self and near-region portions of the surface from the distant region calculation, even though the distant region's tabulation provided only the center coordinates of squares of varying sizes without explicitly listing each square's size, and even though squares in the distant region of varying size bordered on the near region.

Using results from Eqs. D1, D2, and D3, the value of I_V was

$$I_V(x, y) = I_{V0}(x, y) + I_{V1}(x, y) + I_{V2}(x, y). \quad \text{(D5)}$$

APPENDIX E

Program Orientation

A chart of the organization of program PBC shows computer procedures organized in four levels (Fig. 11). Tables IV and V list the function of each procedure.

At the top level is the main program. The main program's function is to call the procedures that organize and execute each type of calculation, e.g., intracellular potentials (CPHII), extracellular potentials (CPHIE), etc. The main program checks flags to determine which procedures to call.

At the second level are the routines that determine the number and locations of field points for each calculation. Field points always were selected at some subset of the nodes. Allocation of most storage in the computer memory also occurred at the second level. Once the x, y coordinates of each field point had been identified, the routine at the second level called a routine at the third level to compute some current or voltage value for that field point. Generally, therefore, the second level routines makes a number of calls to third level, e.g., CIVM made one call to CIVM1 for each of the field points at which I_V is to be computed, passing to CIVM1 as an argument the x, y coordinate of the field point.

At the third level are routines that compute a current or voltage value for a given field point. For example, CIVM1 would compute I_V at a single x, y point. Routines at this third level perform the numerical integrations, for example. Since it is not the case that second-level routines are called in any particular sequence or produce any predetermined set of results in a fixed order, routines at the third level call each other where necessary. For example, CIPHI1 requires values of Φ_i at five points at and near the field point. To obtain these, it makes five calls to PHINT from CIPHI1, rather than assuming these calls previously have been made from CPHI1.

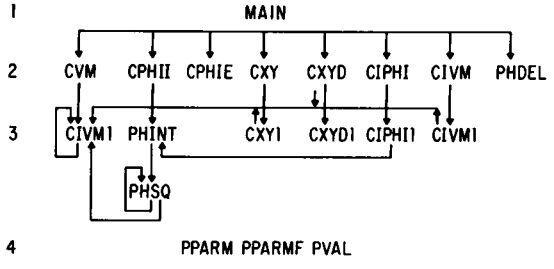

FIGURE 11 Organization of program *PBC*. The lines show the relationship between calling routines and their subprograms. In general, the calling routine controlled the sequence of nodes for which results were to be calculated; the subroutine performed the calculation at each one.

TABLE IV
FUNCTIONS OF MAIN PROGRAM OF PBC

Main program of PBC
- establishes parameter values
- reads corrections to parameter values from input file
- corrects parameter values from input file
- initializes output disk file and writes all parameter values
- calls CVM to calculate values of V_m and $V2$ at all nodes
- calls PHDEL to determine DEL for subdividing grid surface
- calls PHINT to subdivide the grid surface, generating *XCL*, *YCL*, and *FCL*
- If PFLAG = 1 then
  - Calls CPHII to find Φ_i
  - Calls CPHIE to find Φ_e
- If LFLAG = 1 then
  - Calls CXY to find the longitudinal currents
- If DFLAG = 1 then
  - Calls CXYD to find the differences in longitudinal currents
- If IFLAG = 1 then
  - Calls CIPHI to find membrane currents as second derivatives of Φ_i
  - Calls CIVM to find membrane currents from V_m directly.

Routine PHINT uses routine PHSQ the first time PHINT is called to establish list quantities *XCL*, *YCL*, and *FCL*. Thereafter, PHINT computes Φ_i using the list. To ensure that the list is present, routine PHINT is called directly from main when execution starts.

Note that routines CVM1 and PHSQ are recursive. Recursive use is particularly significant for PHSQ, since it provides a mechanism for dynamic subdivision of the geometry of the tissue, as discussed above.

Routines at the fourth level print results and save them on disk files. The MAIN program calls PPARMF to write the parameters on the disk file. All first- and second-level routines use PPARM to print the parameters. All second-level routines use PVAL to print a portion of the computed values, and to save all values computed for $x, y > 0$.

The functions of the main program PBC are given in Table IV, and the functions of each of the subroutines are given in Table V.

Specific Computation Methods. Many calculations require numerical integration over the surface of the tissue. It is useful to recall from Eq. B3 that the calculations can make use of the following list items:

$XCL(LN)$ x-coordinate of the center of each square
$YCL(LN)$ y-coordinate of the center of each square
$$FCL(LN)\ \frac{1}{4\pi G} \cdot \{g_{ox}\partial^2 V_m/\partial x^2 + g_{oy}\partial^2 V_m \partial y^2\} \cdot DX \cdot DY \quad \text{(E1)}$$

where $LN = 1$ to LT, $LT \simeq 25{,}000$ and $\{\ \}$ is evaluated at the center of square LN with edges DX, DY.

Position of Field Points with Respect to Source Surface. In the organization of these calculations, field points were selected as a subset of the nodes located at integral multiple of distance dx or dy (usually 0.1 mm) from the center of the tissue. These nodes also were used as the corners of major squares, and the major squares were subdivided into small squares (Fig. 8).

A result of this organization was that the x coordinate of a field point was never the same as the x coordinate of the center of any square of the subdivided tissue surface, and similarly the y; thereby, numerous special cases could not occur. Furthermore, there was no numerical self-term, i.e., a term where the computed distance from the field point to the center of the source area was zero.

Distances along x and y between the field and source points usually

TABLE V
FUNCTIONS OF SUBROUTINES OF PBC

CIPHI	determines field points where membrane current will be computed from Φ_i. Computes the membrane current by calling CIPHI1
CIPHI1	for a given x, y coordinate, performs numerical differentiation of Φ_i to find membrane current. To find the needed Φ_i values, CIPHI1 calls PHINT five times
CIVM	determines field points where membrane current will be computed directly from V_m. Computes the membrane current by calling CIVM1
CIVM1	finds membrane current I_{VM} directly from V_M by numerical integration. Separates equal anisotrophy case from the general case. For the general case, divides the surface into the self term, near region, and distant region. Uses CVM1 for needed values of $V2$
CPHIE	finds Φ_o by simple subtraction: $\Phi_o = \Phi_i - V_m$
CPHII	determines field points where Φ_i is to be found. To compute each one, PHINT is called
CVM	determines field points where V_m and $V2$ are to be found. To compute values at each one, CVM1 is called
CVM1	analytically calculates the value of V_m for given x, y coordinates. Also finds the first and second derivatives of V_m with respect to x and y as evaluated at the point. Finally, it finds $V2 = g_{ox}\partial^2 V_m/\partial x^2 + g_{oy}\partial^2 V_m/\partial y^2$
CXY	determines field points where longitudinal currents along x and y are to be found and calls CXY1 to find each one
CXY1	determines intracellular and extracellular longitudinal currents along x and y for a given x, y coordinate. Results are called IIX, IIY, IEX, IEY. Uses CVM1 to determine first derivatives of V_m
CXYD	determines field points where differences in longitudinal currents along x and y are to be found and calls CXYD1 to find each one
CXYD1	for given x, y, computes the current along x and y that differs from being equal in magnitude and opposite in direction extracellularly as compared to intracellularly
PHDEL	scans computed values of $V2$ at all nodes and finds DEL, a tolerance used in dynamically subdividing the grid
PHINT	finds Φ_i for a given x, y. Usually Φ_i is calculated by numerical integration using XCL, YCL, and FCL. If these values have not yet been tabulated, PHINT calls PHSQ to subdivide the grid and do the tabulation with one call for each major square
PHSQ	performs a numerical integration over one major square to find that square's contribution to Φ_i. The numerical integration is achieved by subdividing the major square into four subsquares if the corners of the major square have $V2$ values not within DEL. The subsquares are examined recursively to a depth of 6. Final square subdivision is recorded in lists XCL, YCL, and FCL
PPARM	prints values for most parameters in clearly readable form
PPARMF	writes the values for most parameters on the disk file "RESULTS"
PVAL	writes a label parameter and an array parameter both on the printed output and on the disk file "RESULTS." On paper, only some rows, some columns and the diagonal are written. On the disk file, all array entries with either the row or column index greater than or equal to zero are written.

were computed as

$$XD = XCL(LN) - X, \qquad YD = YCL(LN) - Y, \quad \text{(E2)}$$

and these definitions are assumed unless otherwise stated.

APPENDIX F

Longitudinal Currents

The longitudinal current is designated by I with two following subscripts, the first (i or o) indicating intracellular or interstitial and the second direction (x or y). The intracellular currents are found from Eq. 11 and Ohm's law and are simply

$$I_{ix} = -g_{ix}\frac{\partial \Phi_i}{\partial x} = -\frac{g_{ix}}{2\pi G}\int\left[g_{ox}\frac{\partial^2 V_m}{\partial x'^2} + g_{oy}\frac{\partial^2 V_m}{\partial y'^2}\right]\left[\frac{(x-x')}{(x-x')^2 + k(y-y')^2}\right]dx'dy' \quad \text{(F1)}$$

where

$$k = G_x/G_y. \quad \text{(F2)}$$

Similarly

$$I_{iy} = -g_{iy}\frac{\partial \Phi_i}{\partial y} = -\frac{g_{iy}}{2\pi G}\int\left[g_{ox}\frac{\partial^2 V_m}{\partial x'^2} + g_{oy}\frac{\partial^2 V_m}{\partial y'^2}\right]\left[\frac{(y-y')}{(x-x')^2/k + (y-y')^2}\right]dx'dy' \quad \text{(F3)}$$

The interstitial currents can be found once the intracellular currents have been determined since $\Phi_o = \Phi_i - V_m$. We obtain

$$I_{ox} = g_{ox}(I_{ix}/g_{ix} + \partial V_m/\partial x) \quad \text{(F4)}$$

$$I_{oy} = g_{oy}(I_{iy}/g_{iy} + \partial V_m/\partial y). \quad \text{(F5)}$$

An investigation of the integral of Eqs. F1 and F3 shows it to be well-behaved everywhere and, in particular, that it yields zero when integrated through an ϵ neighborhood of the origin. Consequently Eqs. F.1 and F.3 can be fully approximated by discretization over the entire contributing region.

To derive directly the quantities $(I_{ix} + I_{ox})$ and $(I_{iy} + I_{oy})$, an expression for Φ_o comparable with Eq. 11 must be derived from which improved expressions I_{ox} and I_{oy} can be obtained. The derivation of the desired equation follows, by analogy, that of Eq. 11 and is

$$\phi_o(x,y) = \frac{1}{4\pi G}\int\left[g_{ix}\frac{\partial^2 V_m}{\partial x'} + g_{iy}\frac{\partial^2 V_m}{\partial y'^2}\right]\cdot \log\left[\frac{(x-x')^2}{G_x} + \frac{(y-y')^2}{G_y}\right]dx'dy'. \quad \text{(F6)}$$

If we find $I_{oy} = -g_{oy}\partial\Phi_o/\partial y$ and $I_{ox} = -g_{ox}\partial\Phi_o/\partial x$ and combine these results with Eqs. F.1 and F.3 then we have

$$I_{dx} = I_{ix} + I_{ox} = \frac{1}{2\pi G}\int (g_{ox}g_{iy} - g_{ix}g_{oy})\left(\frac{\partial^2 V_m}{\partial y'^2}\right)\left[\frac{(x-x')}{(x-x')^2 + k(y-y')^2}\right]dx'dy' \quad \text{(F7)}$$

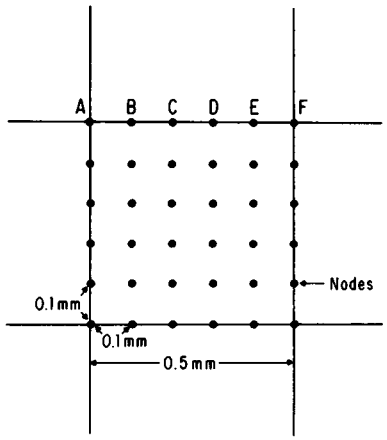

FIGURE 12 Relation of squares used in *PBCC* with nodes used in *PBC*. The dots show the *PBC* nodes. Calculations usually provided a result at each one of these. The squares encompass a collection of nodes whose composite effect was found. The square is the same as those formed by the grid in figures 2–6. Using squares encompassing many nodes was done primarily to provide a more compact result for presentation.

and

$$I_{dy} = I_{iy} + I_{oy} = \frac{1}{2\pi G}\int (g_{oy}g_{ix} - g_{iy}g_{ox}) \left(\frac{\partial^2 V_m}{\partial x'^2}\right)\left[\frac{(y - y')}{(x - x')^2/k + (y - y')^2}\right] dx'dy' \quad \text{(F8)}$$

We note with satisfaction that Eqs. F7 and F8 reduce to zero for isotropic and equal anisotropy conditions. It is interesting to find the x "difference" current to depend on the second derivative of V_m with respect to y, and vice versa for the y "difference" current.

In making figures showing longitudinal and membrane current flow, we computed the composite results for squares 0.5 mm on a side (Fig. 12). Thereby, each such square used computed results for a number of nodes from the original 0.1-mm division into major squares.

Supported by U.S. Public Health Service grants HL 11307, HL 17931, HL 06128, and HL 31286.

Received for publication 14 December 1982 and in final 29 September 1983.

REFERENCES

1. Clerc, L. 1976. Directional differences of impulse spread in trabecular muscle from mammalian heart. *J. Physiol. (Lond.)*. 255:335–346.
2. Schmitt, O. 1969. Biological information processing using the concept of interpenetrating domains. *In* Information Processing in the Nervous System. K. N. Leibovic, editor. Springer-Verlag New York, Inc., New York. 325–531.
3. Miller, W. T., and D. B. Geselowitz. 1978. Simulation studies of the electrocardiogram. *Circ. Res.* 43:301–315.
4. Tung, L. 1978. A bi-domain model for describing ischemic myocardial d-c potentials. Ph.D. Dissertation. Massachusetts Institute of Technology, Cambridge, MA.
5. Roberts, D., L. T. Hersh, and A. M. Scher. 1979. Influence of cardiac fiber orientation on wavefront voltage, conduction velocity, and tissue resistivity in the dog. *Circ. Res.* 44:701–712.
6. Roberts, D., and A. M. Scher. 1982. Effect of tissue anisotropy on extracellular potential fields in canine myocardium in situ. *Circ. Res.* 50:342–351.
7. Peskoff, A. 1979. Electrical potential in three-dimensional electrically syncytial tissues. *Bull. Math. Biol.* 41:163–181.
8. Eisenberg, R. S., V. Barcilon, and R. T. Mathias. 1979. Electrical properties of spherical syncytia. *Biophys. J.* 25:151–180.
9. Spach, M. S., W. T. Miller III, P. C. Dolber, J. M. Kootsey, J. R. Sommer, C. E. Mosher, Jr. 1982. The functional role of structural complexities in the propagation of depolarization in the atrium of the dog. *Circ. Res.* 50:175–191.
10. Barr, L., and E. Jakobbson. 1976. The spread of current in electrical syncytia. *In* Physiology of Smooth Muscle. E. Bulbring and M. F. Shuba, editors. Raven Press, New York. 41–48.
11. Muler, A. L., and V. S. Markin. 1978. Electrical properties of anisotropic nerve-muscle syncytia. III. Steady form of the excitation front. *Biophysics.* 22:699–704.
12. Plonsey, R., and Y. Rudy. 1980. Electrocardiogram sources in a 2-dimensional anisotropic activation model. *Med. Biol. Eng. Comp.* 18:87–94.
13. Plonsey, R., and R. E. Collin. 1961. Principles and Applications of Electromagnetic Fields. McGraw-Hill Inc., New York. 33–35.
14. Hodgkin, A. L., and W. A. Rushton. 1946. The electrical constants of a crustacean nerve fiber. *Proc. R. Soc. Biol. Sci.* 133:444.
15. Geselowitz, D., R. C. Barr, M. S. Spach, and W. T. Miller, III. 1982. The impact of adjacent isotropic fluids on electrograms from anisotropic cardiac muscle: a modelling study. *Circ. Res.* 51:602–613.
16. Spach, M. S. 1982. The electrical representation of cardiac muscle based on discontinuities of axial resistivity at a microscopic and macroscopic level. *In* Normal and Abnormal Conduction in the Heart. A. Paes de Carvalho, B. E. Hoffman, and M. Lieberman editors. Futura Publishing Co., Inc., Mount Kisco, NY. 145–179.
17. Spach, M. S., R. C. Barr, G. S. Serwer, E. A. Johnson, and J. M. Kootsey. 1971. Collision of excitation waves in the dog Purkinje System. *Circ. Res.* 29:499–511.
18. Ushiyama, J. 1971. Cardiac action potentials recorded from the site at which two impulses of excitation have collided. *In* Research in Physiology. A Liber Memorialis in Honor of Professor Chandler McCuskey Brooks. F. F. Kao, K. Koizumi, and M. Vassalle, editors. Auto Gaggi, Bologna, Italy. 37–43.